Twisted bilayer BC₃: Valley interlocked anisotropic flat bands

Toshikaze Kariyado ⬤

International Center for Materials Nanoarchitectonics, National Institute for Materials Science, Tsukuba 305-0044, Japan

Here we propose BC₃, a graphene derivative that has been synthesized, as a platform to realize exotic quantum phases by introducing a moiré pattern with mismatched stacking. In twisted bilayer BC₃, it is shown that a crossover from two-dimensional to quasi-one-dimensional (quasi-1D) band structure takes place with the twist angle as a control parameter. This is a typical manifestation of the guiding principle in van der Waals stacked systems: The quantum interference between Bloch wave functions in adjacent layers has a striking effect on the effective interlayer tunneling. Interestingly, quasi one dimensionalization happens in a valley-dependent manner. Namely, there is interlocking between the valley index and the quasi-1D directionality, which makes BC₃ a plausible candidate for valleytronics devices. In addition, the strongly correlated regime of the valley interlocked quasi-1D state reduces to an interesting variant of the Kugel-Khomskii model where intertwined valley and spin degrees of freedom potentially induce exotic quantum phases. Notably, this variant of the Kugel-Khomskii model cannot be realized in conventional solids due to the threefold valley degeneracy.

I. INTRODUCTION

Nanoscale moiré patterns in van der Waals (vdW) heterostructures [1] with small interlayer mismatches are currently attracting much attention as a key to manipulate electrons artificially. A typical setup to realize a tunable moiré pattern is a bilayer system with angle misalignment between the layers, known as a twisted bilayer system [2–23]. A moiré-patterned bilayer system is featured by its position dependence of the relation between two layers, which induces position dependence of the effective interlayer tunneling and the electrostatic potential from the partner layers. Generically, spatial profiles of the tunneling and electrostatic potential affect the motion of electrons, allowing us to control the electronic band structures by modulating the moiré pattern, say, by changing the twist angle.

Regarding spatial profiles of the interlayer tunneling, the quantum interference between the Bloch wave functions in the two layers plays an essential role [24]. Notably, if the focused state has finite lattice momentum in each layer, the spatial profile of the effective tunneling may not follow the crystalline symmetry of the underlying lattice due to the interference effects, which potentially leads to interesting phenomena such as anisotropic band flattening. In this perspective, a multivalley system, which is featured by degeneracy between the states with different momenta, is an interesting building block for twisted bilayers. The valley degrees of freedom are well defined and practically conserved if the moiré pattern is smooth enough for electrons to suppress the intervalley scattering with large momentum transfer. If we can manipulate an electronic structure of a multivalley twisted bilayer in a valley-dependent manner, it paves a way to build moiré-based valleytronics [25] devices.

Amongst two-dimensional (2D) atomic layer materials, graphene derivatives are interesting and important in the vdW

heterostructure framework. One example is monolayer BC₃, where a quarter of the carbon atoms in graphene are replaced by boron atoms in an arrangement depicted in Fig. 1(a). This structure preserves the space group symmetry of graphene but forms a 2×2 supercell. This BC₃ monolayer sheet has been synthesized on the NbB₂(0001) surface [26,27], and some experimental characterizations have been worked out [28,29]. It is predicted to be a 2D semiconductor, i.e., the first-principles calculation shows a band gap at the Fermi energy [30–36]. Notably, the conduction bottom is at the M point, showing anisotropic electronlike parabolic band dispersion. There are three symmetrically related M points in the Brillouin zone due to the space group symmetry of this system, which means that monolayer BC₃ is a three-valley system. Having multiple valleys on high-symmetry points in the Brillouin zone makes BC₃ a promising candidate for realizing valleytronics with the vdW heterostructure framework.

In this paper, electronic properties of twisted bilayer BC₃ are investigated. For this purpose, we build two types of effective models, a tight-binding model and a continuum model, to have clear and intuitive understanding of the results by comparison. The parameters required in the effective models are fixed within the *local approximation*, which stands on the fact that the atomic structure in a slightly twisted bilayer is *locally* well approximated by the one in an untwisted bilayer system with in-plane displacement. Since the first-principles calculations can be applied on the untwisted bilayer without huge computational costs, it is used to fix the parameters in the effective models (see Fig. 3 for the strategy to derive the effective models). It is revealed that both the tight-binding model and the continuum model consistently show valley-dependent anisotropic band flattening, in which originally 2D band dispersion is squeezed into a quasi-one-dimensional (1D) one with valley-dependent dispersive directions upon twist. This valley interlocking quasi-1D dispersion indicates
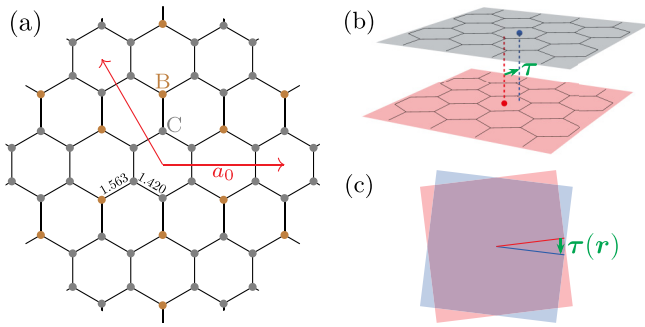
FIG. 1. (a) Schematic picture for the crystal structure of monolayer BC$_3$. The monolayer lattice constant a_0 is 5.167 Å. The C-C and B-C distances are 1.420 and 1.563 Å, respectively. (b) and (c) Schematic illustrations of the in-plane displacement τ for the untwisted case (b) and the position-dependent $\tau(r)$ for the twisted case (c).

valley-dependent transport, which makes twisted bilayer BC$_3$ useful for valleytronics devices. Having the valleytronics application in mind, we also discuss possible valley selection by linearly polarized light.

In addition to the band dispersion manipulation at the noninteracting level, the strongly correlated regime of the twisted bilayer BC$_3$ is also investigated. It is shown that the strong coupling limit of the three-valley effective model at the filling of one electron per moiré unit cell leads to a three-orbital variant of the Kugel-Khomskii model, in which a characteristic valley-spin coupling gives rise to quantum phases with intertwined valleys and spins. Notably, a model with the same symmetry as this generalized Kugel-Khomskii model cannot be realized in a conventional solid, due to the threefold valley degeneracy at the small angle limit where the valley degrees of freedom decouple.

The paper is organized as follows. First, we introduce effective models and explain how to fix the required parameters within the local approximation. Next, crystalline and electronic structures for monolayer and bilayer systems are shown in order. Then, we discuss the valley selection by linearly polarized light and provide analysis in the strongly correlated regime before the summary and final discussion.

II. METHODS

A. Local approximation

To build effective models for analyzing the electronic structure of BC$_3$, we mostly rely on the *local approximation* [37]. In the local approximation, we make full use of the fact that a crystal structure of a twisted bilayer is *locally* well approximated by its untwisted counterpart for small twist angles. The untwisted bilayers can be analyzed without huge computational resources, since the unit cell size is conserved in untwisted cases.

One of the important parameters to characterize a given untwisted bilayer is an in-plane displacement τ of the upper layer relative to the lower layer [Fig. 1(b)]. Then, the essence of the moiré structure is the position dependence of τ. In the case of a twisted bilayer, τ depends on the position

as [38]

$$\tau(r) = 2\sin\frac{\phi}{2}\hat{z} \times r, \tag{1}$$

where ϕ is a twist angle, $\hat{z}$ is a unit vector perpendicular to the 2D system, and r is an in-plane position measured from the rotation center [see Fig. 1(c)]. When $\tau(r)$ for two different positions, say, r' and r'', differ only by a lattice vector $n_1 a_1 + n_2 a_2$ (where n_i are integers and a_i are unit vectors of the monolayer), r' and r'' are identified in terms of the moiré pattern, giving us unit vectors for the moiré pattern L_i as

$$L_i = \frac{\hat{z} \times a_i}{2\sin\frac{\phi}{2}}. \tag{2}$$

Then, writing a spatial position as $r = r_1 L_1 + r_2 L_2$ and introducing $\tau_i(r)$ as $\tau(r) = \tau_1(r)a_1 + \tau_2(r)a_2$, Eq. (1) results in [24,37]

$$\tau_i(r_i) = -r_i. \tag{3}$$

This means that scanning over the moiré unit cell corresponds to scanning over all possible τ in the monolayer unit cell.

When the electronic structure of each layer is effectively approximated by a single band model, the most important effect of constructing a bilayer is interlayer tunneling, which generically lifts the band degeneracy caused by layer doubling. Specifically, τ dependence of the splitting (and the shift of the average energy) of the target band gives important information. For untwisted bilayers, energy splitting and shift can be derived for each momentum k in the original Brillouin zone, since the unit cell size is conserved. For later use, we write this τ-dependent splitting and shift as $2\Delta_k(\tau)$ and $\epsilon_k(\tau)$, respectively.

Generically, the position dependence of τ induces the position dependence of the interlayer distance, or corrugation [39]. In the small (but not too small) twist angle limit, this position dependence of the interlayer distance is expected to be captured by the τ dependence of the interlayer distance in the untwisted bilayers. Taking this approximation, in the following, we first derive the τ-dependent interlayer distance $d_z(\tau)$ and use that information to investigate the electronic properties. If the twist angle is too small, each layer can experience in-plane distortions, but this is beyond our current scope.

B. Effective models

As we have noted, we are going to build two complementary effective models for BC$_3$, a tight-binding model and a $(k \cdot p)$-type continuum model. Let us start by introducing a monolayer tight-binding model, which involves π electrons, or p_z orbitals of B and C atoms. Although we have two species of the p_z orbitals, from B or C, there is only one orbital per site, allowing us to identify the site index and the orbital index. Then, the Hamiltonian for the monolayer tight-binding model is written as

$$H_{\text{mono}}^{\text{TB}} = \sum_{ij} t_{ij} c_i^\dagger c_j, \tag{4}$$

where c_i ($c_i^\dagger$) is the annihilation (creation) operator for the ith site. Since a unit cell contains eight sites (six C atoms and two B atoms), this results in an eight-band model.

Assuming a very simple form of interlayer hoppings, we can lift this monolayer tight-binding model to a bilayer tight-binding model as

$$H^{\mathrm{TB}} = \sum_{ij\alpha}[t_{ij}c_{i\alpha}^\dagger c_{j\alpha} + t_{\mathrm{inter}}(\boldsymbol{r}_i - \boldsymbol{r}_j)c_{i\alpha}^\dagger c_{j\bar\alpha}], \quad (5)$$

where $\boldsymbol{r}_i$ is the position of the ith site and α specifies the layer (upper or lower) with $\bar\alpha$ denoting the opposite layer of α. Here, our simple assumption is that the interlayer hopping only depends on the relative position between the two sites. We even neglect the difference between the atom species B and C, but later it turns out to be sufficient for our purpose. Formally, Eq. (5) can be used for both the twisted and the untwisted bilayers, but of course the position of each site is different for the two cases, resulting in different periodicity.

For the ($\boldsymbol{k} \cdot \boldsymbol{p}$)-type continuum model, we focus on the conduction bottom at the M_i point. For the valley M_i, the monolayer continuum Hamiltonian becomes

$$H_{\mathrm{mono}}^{(i)}(\boldsymbol{k}) = \epsilon_0 + \frac{\hbar^2}{2m_\parallel}\big((\boldsymbol{k}-\boldsymbol{\kappa}_i)\cdot\boldsymbol{e}_i^\parallel\big)^2 + \frac{\hbar^2}{2m_\perp}(\boldsymbol{k}\cdot\boldsymbol{e}_i^\perp)^2, \quad (6)$$

where $\boldsymbol{\kappa}_i$ is the momentum for the M_i point and $\boldsymbol{e}_i^{\parallel,\perp}$ are unit vectors parallel and perpendicular to $\boldsymbol{\kappa}_i$. Because of the symmetry at the M points, the relevant mass tensor is fixed by two parameters, $m_\perp$ and $m_\parallel$.

The continuum Hamiltonian for the untwisted bilayers for the M_i valley can now be written as [38,40]

$$H^{(i)}(\boldsymbol{k}, \boldsymbol{\tau}) = \begin{pmatrix} H_{\mathrm{mono}}^{(i)}(\boldsymbol{k}) + U_{\boldsymbol{k}}(\boldsymbol{\tau}) & V_{\boldsymbol{k}}(\boldsymbol{\tau}) \\ (V_{\boldsymbol{k}}(\boldsymbol{\tau}))^\dagger & H_{\mathrm{mono}}^{(i)}(\boldsymbol{k}) + U_{\boldsymbol{k}}(\boldsymbol{\tau}) \end{pmatrix}, \quad (7)$$

which is valid for $\boldsymbol{k} \sim \boldsymbol{\kappa}_i$. Here, $V_{\boldsymbol{k}}(\boldsymbol{\tau})$ represents the interlayer tunneling, while $U_{\boldsymbol{k}}(\boldsymbol{\tau})$ is contributed from the electrostatic potential from the partner layer and the multiband effects such as virtual hopping to the other bands. Both $V_{\boldsymbol{k}}(\boldsymbol{\tau})$ and $U_{\boldsymbol{k}}(\boldsymbol{\tau})$ depend on $\boldsymbol{k}$ and $\boldsymbol{\tau}$. Since the energy eigenvalues of Eq. (7) are

$$E_\pm^{(i)}(\boldsymbol{k}, \boldsymbol{\tau}) = H_{\mathrm{mono}}^{(i)}(\boldsymbol{k}, \boldsymbol{\tau}) + U_{\boldsymbol{k}}(\boldsymbol{\tau}) \pm |V_{\boldsymbol{k}}(\boldsymbol{\tau})|, \quad (8)$$

$V_{\boldsymbol{k}}(\boldsymbol{\tau})$ and $U_{\boldsymbol{k}}(\boldsymbol{\tau})$ can be related to the energy split $2\Delta_{\boldsymbol{k}}(\boldsymbol{\tau})$ and shift $\epsilon_{\boldsymbol{k}}(\boldsymbol{\tau})$ as [37]

$$\Delta_{\boldsymbol{\kappa}_i}(\boldsymbol{\tau}) = |V_{\boldsymbol{\kappa}_i}(\boldsymbol{\tau})|, \quad \epsilon_{\boldsymbol{\kappa}_i}(\boldsymbol{\tau}) = \epsilon_0 + U_{\boldsymbol{\kappa}_i}(\boldsymbol{\tau}). \quad (9)$$

Lastly, the continuum Hamiltonian for the twisted bilayers can be written as [2,5,7]

$$H^{(i)} = \begin{pmatrix} H_+^{(i)}(-i\nabla) + U^{(i)}(\boldsymbol{r}) & V^{(i)}(\boldsymbol{r}) \\ (V^{(i)}(\boldsymbol{r}))^\dagger & H_-^{(i)}(-i\nabla) + U^{(i)}(\boldsymbol{r}) \end{pmatrix}, \quad (10)$$

where $H_\pm^{(i)}$ is $H_{\mathrm{mono}}^{(i)}$ rotated by $\pm\phi/2$. In order to take account of the spatial dependence of $U^{(i)}(\boldsymbol{r})$ and $V^{(i)}(\boldsymbol{r})$, $\boldsymbol{k}$ in $H_{\mathrm{mono}}^{(i)}$ is replaced by $-i\nabla$. The remaining task is to fix $U^{(i)}(\boldsymbol{r})$ and $V^{(i)}(\boldsymbol{r})$. In the twisted bilayer, the large-scale moiré pattern indicates that the Brillouin zone is folded into a small moiré Brillouin zone, and if we further limit ourselves to a small energy range, it typically turns out that the target state is mostly
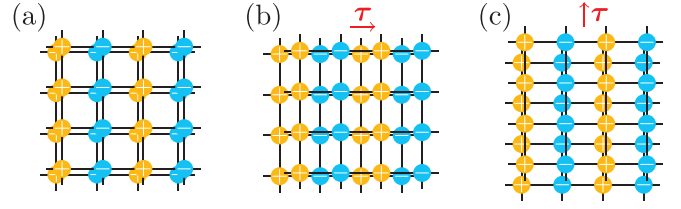

FIG. 2. Schematic illustrations of interference effects. As an example, we think of the case where the in-plane momentum gives a stripelike + and − phase pattern in the Bloch wave function (a). When one of the layers is shifted in the lateral direction by half a unit cell length (b), the closely packed chain of atoms has phase alternation along the chain, canceling out interlayer tunneling due to the quantum interference, but when the shift direction is vertical (c), no strong cancellation of interlayer tunneling occurs.

contributed from a small region around a certain momentum in the original Brillouin zone. In our case, Eq. (6) suggests that $\boldsymbol{\kappa}_i$ is regarded as the "certain momentum." Then, a possible approximation is to set

$$U^{(i)}(\boldsymbol{r}) = U_{\boldsymbol{\kappa}_i}(\boldsymbol{\tau}(\boldsymbol{r})), \quad V^{(i)}(\boldsymbol{r}) = V_{\boldsymbol{\kappa}_i}(\boldsymbol{\tau}(\boldsymbol{r})). \quad (11)$$

Note that the position dependence is included through the spatial dependence of $\boldsymbol{\tau}$ under the twist.

Combining Eqs. (9) and (11), we can fix $U^{(i)}(\boldsymbol{r})$ by $\epsilon_{\boldsymbol{\kappa}_i}(\boldsymbol{\tau})$. On the other hand, $\Delta_{\boldsymbol{\kappa}_i}(\boldsymbol{\tau})$ can fix $V_{\boldsymbol{\kappa}_i}(\boldsymbol{\tau})$ only up to the phase ambiguity, and therefore, in practice, we derive an approximate $V_{\boldsymbol{\kappa}_i}(\boldsymbol{\tau})$ using the tight-binding model. Specifically, using the Bloch wave function $\psi_{\boldsymbol{\kappa}_i}(\boldsymbol{r})$ for the target band obtained in the tight-binding model, we use [10,15,38,41–43]

$$V_{\boldsymbol{\kappa}_i}(\boldsymbol{\tau}) = e^{-i\boldsymbol{\kappa}_i\cdot\boldsymbol{\tau}}\sum_{ij}\psi_{\boldsymbol{\kappa}_i}^*(\boldsymbol{r}_i)t_{\mathrm{inter}}(\boldsymbol{r}_i - \boldsymbol{r}_j - \boldsymbol{\tau})\psi_{\boldsymbol{\kappa}_i}(\boldsymbol{r}_j), \quad (12)$$

which corresponds to the interlayer tunneling calculated at the lowest order in $t_{\mathrm{inter}}(\boldsymbol{r})$.

Equation (12) tells us that the quantum interference associated with spatial structures of Bloch phase has a striking effect on the tunneling amplitude [24,40]. Let us see this through a schematic model in Fig. 2. This is a stack of two layers, and we assume that each layer has in-plane momentum giving a stripelike Bloch phase pattern [Fig. 2(a)]. Then, consider that we introduce a half-unit-length shift between layers in the lateral [Fig. 2(b)] and vertical [Fig. 2(c)] directions. In Figs. 2(b) and 2(c), we see closely packed chains of atoms lying laterally and vertically, respectively. In the case of the lateral shift [Fig. 2(b)], each of the closely packed chains of atoms shows phase alternation along the chain, leading to the suppressed interlayer tunneling due to the quantum interference. On the other hand, in the case of the vertical shift [Fig. 2(c)], the closely packed chains of atoms do not show phase alternation along the chains, indicating that no significant quantum interference is in effect. After applying the mapping between the $\boldsymbol{\tau}$ dependence and the $\boldsymbol{r}$ dependence in the moiré pattern, the difference between the lateral and the vertical shifts generates a quasi-1D pattern in the effective tunneling amplitude. This is the mechanism behind the anisotropic band flattening in twisted bilayer BC₃ shown below.
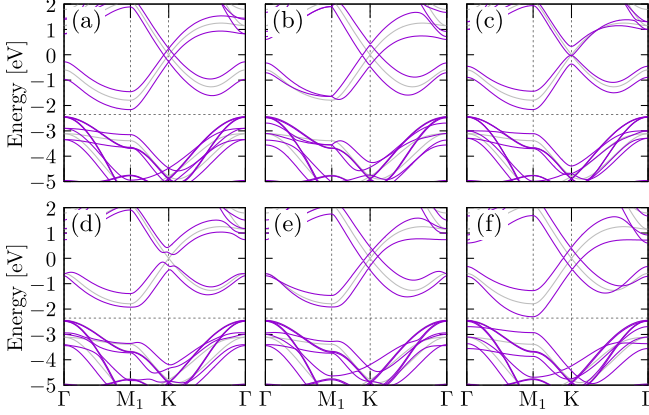
FIG. 3. Schematic illustration of the theoretical framework. The gray (white) boxes are for the models with (without) moiré superstructure. The blue boxes denote the quantities derived in the numerical calculation. The red box shows the empirically given function where the required parameters are chosen to optimize $\Delta^{\mathrm{TB}}(\boldsymbol{\tau})$. The labels '1' to '9' correspond to 'procedure 1' to "procedure 9" in the main text.

C. Theoretical and numerical scheme

Our scheme to fix the required parameters in each of the effective models is summarized in Fig. 3. We start with applying the first-principles density functional theory (DFT) on monolayer BC_3 ("*ab initio* DFT" in Fig. 3). We first perform the lattice relaxation to obtain the crystalline parameters for the monolayer. Then, we derive the maximally localized (MaxLoc) Wannier functions to obtain the monolayer tight-binding model (procedure 1 in Fig. 3). The effective mass used in the continuum model can be derived from the band structure obtained either in DFT or in the tight-binding model (procedure 2 in Fig. 3).

For the bilayers, we start with deriving $d_z(\boldsymbol{\tau})$ by DFT (procedure 3 in Fig. 3; see Appendix B for details). Using the obtained $d_z(\boldsymbol{\tau})$ as an input, we calculate $\epsilon_{\kappa_i}(\boldsymbol{\tau})$ and $\Delta_{\kappa_i}(\boldsymbol{\tau})$ by DFT (procedure 4 in Fig. 3) as references for the following analysis. A tight-binding model for the untwisted bilayer ("bilayer tight-binding" in Fig. 3) requires in-plane hopping parameters and reasonable $t_{\mathrm{inter}}(\boldsymbol{r})$ (procedure 5 in Fig. 3), and a reasonable choice is made by calculating $\epsilon_{\kappa_i}(\boldsymbol{\tau})$ and $\Delta_{\kappa_i}(\boldsymbol{\tau})$ within the tight-binding model [$\epsilon_0^{\mathrm{TB}}(\boldsymbol{\tau})$ and $\Delta^{\mathrm{TB}}(\boldsymbol{\tau})$ in Fig. 3] and adjusting $t_{\mathrm{inter}}(\boldsymbol{r})$ to have consistency between $\Delta^{\mathrm{TB}}(\boldsymbol{\tau})$ and $\Delta^{\mathrm{DFT}}(\boldsymbol{\tau})$ (procedure 6 in Fig. 3). The adjusted $t_{\mathrm{inter}}(\boldsymbol{\tau})$ is plugged into Eq. (12) to have $V_{\kappa_i}(\boldsymbol{\tau})$ (procedure 7 in Fig. 3), and the ($\boldsymbol{k} \cdot \boldsymbol{p}$)-type continuum model for the twisted bilayer ("moiré bilayer $\boldsymbol{k} \cdot \boldsymbol{p}$") is obtained using the derived effective mass and $V_{\kappa_i}(\boldsymbol{\tau})$ (procedure 8 in Fig. 3). Alternatively, the adjusted $t_{\mathrm{inter}}(\boldsymbol{r})$ is transported to the tight-binding model for twisted bilayers ("moiré bilayer tight-binding" in Fig. 3) through Eq. (5) (procedure 9 in Fig. 3). We can cross-check the results under moiré structures by comparing the moiré bilayer tight-binding model and the moiré bilayer $\boldsymbol{k} \cdot \boldsymbol{p}$ model.

III. RESULTS

A. Monolayer

Let us start with the crystal structure analysis. The crystal structure of BC_3 [see Fig. 1(a)] is fixed by three parameters: the in-plane lattice constant a_0, the C-C distance $d_{\text{C-C}}$, and the B-C distance $d_{\text{B-C}}$. They are obtained as $a_0 = 5.167$ Å, $d_{\text{C-C}} =$

FIG. 4. (a) Unit cells and Brillouin zones with (orange) and without (cyan) a moiré superlattice for BC_3. These are shown to see the angle and directions, i.e., the actual sizes are very different for unit cells and Brillouin zones with and without moiré superstructures. (b) Band structure obtained with the first-principles method (gray lines), and band structure for the monolayer tight-binding model derived by the maximally localized Wannier function method (green lines).

1.420 Å, and $d_{\text{B-C}} = 1.563$ Å, respectively, consistent with previous experimental [26] and theoretical studies [31,32,34–36,44–46].

The electronic band structure obtained by DFT with the above crystal parameters is shown as the gray lines in Fig. 4(b). There is a band gap at the Fermi energy (indicated as the horizontal dashed line), and the conduction bottom, on which we are going to focus, is located at the M point showing the electronlike parabolic dispersion. At the K point, we find a Dirac cone above the Fermi energy inherited from the pristine graphene. All of these features are consistent with previous theoretical studies [30–32]. (Note that both the Heyd-Scuseria-Ernzerhof functional [33,34,36] and the one-shot GW approximation [35] give a larger band gap, but still the band shapes are similar to the Perdew-Burke-Ernzerhof generalized gradient approximation (PBE-GGA) results.) As a technical note, we set the zero of energy at the energy of the Dirac cone center for the monolayer throughout the paper.

Next, we build a tight-binding model with eight p_z orbitals, six on C atoms and two on B atoms, using the WANNIER90 package [47,48] (procedure 1 in Fig. 3; see Appendix C for details). The band structure of the obtained monolayer tight-binding model is shown by the green lines in Fig. 4(b). It shows a good match to the DFT band structure near the Fermi energy, including the structure around the conduction bottom at the M point, which is of interest to us.

From the calculated band structure, the effective mass required for the continuum models can also be derived: $m_\parallel$ and $m_\perp$ are obtained by estimating the curvature of the band at the conduction bottom at the M point (procedure 2 in Fig. 3). The results are $m_\parallel = 1.36 m_e$ and $m_\perp = 0.15 m_e$, where m_e is the bare electron mass, which is consistent with previous work [35].

B. Untwisted bilayer

To build models for bilayers, we start with deriving the $\boldsymbol{\tau}$ dependence of the interlayer distance (procedure 3 in Fig. 3).

FIG. 5. Band structures for untwisted bilayers with selected $\boldsymbol{\tau}$ obtained by the first-principles method. The horizontal dashed line represents the original Fermi level. (a), (b), (c), (d), (e), and (f) correspond to $(\tau_1, \tau_2) = (0, 0)$, $(1/2, 0)$, $(2/3, 1/3)$, $(1/3, 1/3)$, $(0, 1/3)$, and $(0, 1/2)$, respectively.

For this purpose, we use DFT and employ the rigid-layer approximation where the interlayer distance for each $\boldsymbol{\tau}$ is determined by minimizing the total energy while the crystalline parameters for each layer are frozen. Note that the full lattice relaxation does not fit our purpose, since it automatically chooses stable (or metastable) $\boldsymbol{\tau}$, preventing the scan over all possible $\boldsymbol{\tau}$. It turns out that $d_z(\boldsymbol{\tau})$ is satisfactorily approximated by a simple function

$$
\begin{aligned}
d_z(\boldsymbol{\tau}) = {} & c_1 + c_2(\cos\tau_1 + \cos\tau_2 + \cos(\tau_1 - \tau_2)) \\
& + c_3(\cos(\tau_1 + \tau_2) + \cos(\tau_1 - 2\tau_2) + \cos(2\tau_1 - \tau_2)) \\
& + c_4(\cos(2\tau_1) + \cos(2\tau_2) + \cos(2\tau_1 - 2\tau_2)),
\end{aligned} \quad (13)
$$

with $\{c_1, c_2, c_3, c_4\} = \{3.361\,\text{Å}, 0.025\,\text{Å}, 0.077\,\text{Å}, 0.015\,\text{Å}\}$. (See Appendix B for details.)

Using $d_z(\boldsymbol{\tau})$ as the interlayer distance for each $\boldsymbol{\tau}$, we inspect the $\boldsymbol{\tau}$ dependence of the electronic band structure focusing on how the interlayer tunneling modifies the band structure. Figure 5 shows the band structures of monolayers (the gray lines) and bilayers (the purple lines) for the selected $\boldsymbol{\tau}$ obtained within DFT. (For some $\boldsymbol{\tau}$, the bilayer band structures can be found in the literature [32,35].) The bands are split and shifted in the bilayers with $\boldsymbol{\tau}$ dependence. In our analysis, the $\boldsymbol{\tau}$ dependence of the split and the shift of the conduction bottom at the M point is important. The split is extracted as $\Delta^{\mathrm{DFT}}_{\kappa_i}(\boldsymbol{\tau}) = (E_2(\kappa_i, \boldsymbol{\tau}) - E_1(\kappa_i, \boldsymbol{\tau}))/2$ while the shift is extracted as $\epsilon^{\mathrm{DFT}}_{\kappa_i}(\boldsymbol{\tau}) = (E_1(\kappa_i, \boldsymbol{\tau}) + E_2(\kappa_i, \boldsymbol{\tau}))/2$, where $E_1(\kappa_i, \boldsymbol{\tau})$ and $E_2(\kappa_i, \boldsymbol{\tau})$ are the energies of the lowest and the second lowest conduction band at the M_i point, respectively (procedure 4 in Fig. 3). $\Delta^{\mathrm{DFT}}_{\kappa_1}(\boldsymbol{\tau})$ and $\epsilon^{\mathrm{DFT}}_{\kappa_1}(\boldsymbol{\tau})$ for the M_1 point are plotted in Figs. 6(a) and 6(b) by the purple dots. For $\Delta^{\mathrm{DFT}}_{\kappa_1}(\boldsymbol{\tau})$, we also show its contour plot on the $\boldsymbol{\tau}$ space in Fig. 6(c). Because of the interference between the Bloch wave functions in the upper and the lower layers, there appears a characteristic quasi-one-dimensional dip structure in $\Delta^{\mathrm{DFT}}_{\kappa_1}(\boldsymbol{\tau})$. The direction of the quasi-1D dip depends on the valley, i.e., $\Delta^{\mathrm{DFT}}_{\kappa_i}(\boldsymbol{\tau})$ for the M_2 (M_3) point is obtained by rotating $\Delta^{\mathrm{DFT}}_{\kappa_1}(\boldsymbol{\tau})$ in Fig. 6(c) by 60° (120°). This valley-dependent quasi-1D structure plays a crucial role in the later discussions.
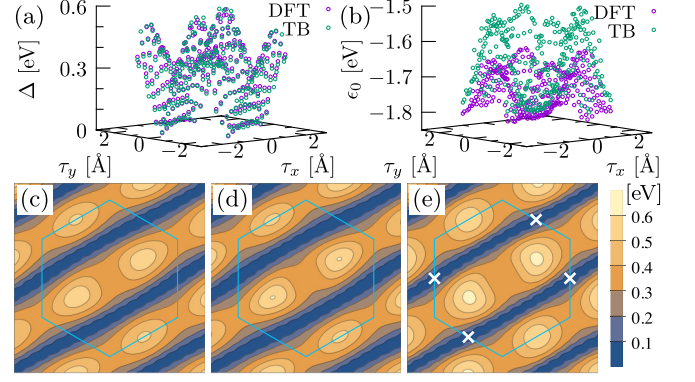
FIG. 6. (a) and (b) Interlayer-coupling-induced (a) gap $\Delta(\boldsymbol{\tau})$ and (b) mean energy shift $\epsilon_0(\boldsymbol{\tau})$. The results obtained by the first-principles method (DFT) and by the tight-binding model with empirical interlayer hopping (TB) are compared. We choose the parameters in the empirical interlayer hopping to match $\Delta^{\mathrm{DFT}}(\boldsymbol{\tau})$ and $\Delta^{\mathrm{TB}}(\boldsymbol{\tau})$, and (a) shows that the choice is reasonable. $\epsilon^{\mathrm{DFT}}_0(\boldsymbol{\tau})$ and $\epsilon^{\mathrm{TB}}_0(\boldsymbol{\tau})$ are similar in shape, but with a bit different energy scale. (c)–(e) Contour plots for (c) $\Delta^{\mathrm{DFT}}(\boldsymbol{\tau})$, (d) $\Delta^{\mathrm{TB}}(\boldsymbol{\tau})$, and (e) $|V_{\kappa_1}(\boldsymbol{\tau})|$.

For the bilayer tight-binding model, the intralayer hopping t_{ij} has already been derived, and the remaining task is to determine the interlayer hopping $t_{\mathrm{inter}}(\boldsymbol{r})$. In this paper, a simple form,

$$
t_{\mathrm{inter}}(\boldsymbol{r}) = h_0 \exp\left(-\frac{2d_0(r_z - d_0)}{r_0^2}\right) \exp\left(-\frac{r_x^2 + r_y^2}{r_0^2}\right), \quad (14)
$$

is assumed where $d_0 = d_z(\mathbf{0})$. We set r_0 and h_0 as 2.0 Å and 0.30 eV, respectively. Just as in the case of DFT, we derive the split $\Delta^{\mathrm{TB}}_{\kappa_i}(\boldsymbol{\tau})$ and the shift $\epsilon^{\mathrm{TB}}_{\kappa_i}(\boldsymbol{\tau})$ by the energies of the lowest and the second lowest conduction band at the M_i point in the tight-binding model. $\Delta^{\mathrm{TB}}_{\kappa_1}(\boldsymbol{\tau})$ and $\epsilon^{\mathrm{TB}}_{\kappa_1}(\boldsymbol{\tau})$ for the M_1 point are plotted in Figs. 6(a) and 6(b) by the green dots. Also, Fig. 6(d) shows the contour plot of $\Delta^{\mathrm{TB}}_{\kappa_1}(\boldsymbol{\tau})$. As Figs. 6(a)–6(d) show, $\Delta^{\mathrm{TB}}_{\kappa_i}(\boldsymbol{\tau})$ well compares with $\Delta^{\mathrm{DFT}}_{\kappa_i}(\boldsymbol{\tau})$, despite the simple form of $t_{\mathrm{inter}}(\boldsymbol{r})$. Since the parameters are chosen to have a good match between $\Delta^{\mathrm{TB}}_{\kappa_i}(\boldsymbol{\tau})$ and $\Delta^{\mathrm{DFT}}_{\kappa_i}(\boldsymbol{\tau})$, we find some quantitative difference for $\epsilon_{\kappa_i}(\boldsymbol{\tau})$. However, the overall structures, or the qualitative features, of the $\boldsymbol{\tau}$ dependence are common to $\epsilon^{\mathrm{TB}}_{\kappa_i}(\boldsymbol{\tau})$ and $\epsilon^{\mathrm{DFT}}_{\kappa_i}(\boldsymbol{\tau})$.

Once the interlayer hopping $t_{\mathrm{inter}}(\boldsymbol{r})$ is fixed, it is possible to have $V_{\kappa_i}(\boldsymbol{\tau})$ through Eq. (12). Figure 6(e) is the contour plot of $|V_{\kappa_1}(\boldsymbol{\tau})|$ in the $\boldsymbol{\tau}$ space, which shows a satisfactory match to Fig. 6(d). The reason for the satisfactory but imperfect matching is that Eq. (12) is derived at the lowest order in $t_{\mathrm{inter}}(\boldsymbol{r})$. The previous theory on symmetry-based constraints on $V_k(\boldsymbol{\tau})$ [24,40] guarantees that $V_{\kappa_1}(\boldsymbol{\tau})$ vanishes at the points marked by white crosses in Fig. 6(e).

C. Twisted bilayer

Using $\epsilon^{\mathrm{TB}}_{\kappa_i}(\boldsymbol{\tau})$ and $V_{\kappa_i}(\boldsymbol{\tau})$ obtained in the previous section, $U^{(i)}(\boldsymbol{r})$ and $V^{(i)}(\boldsymbol{r})$ in the continuum Hamiltonian (10) are fixed through Eqs. (9) and (11). The energy band structure for this continuum model can be calculated by the plane wave expansion method. The obtained band dispersions for $\phi = 7.34°$ and 5.09° are shown in Figs. 7(a) and 7(d), respectively. In the
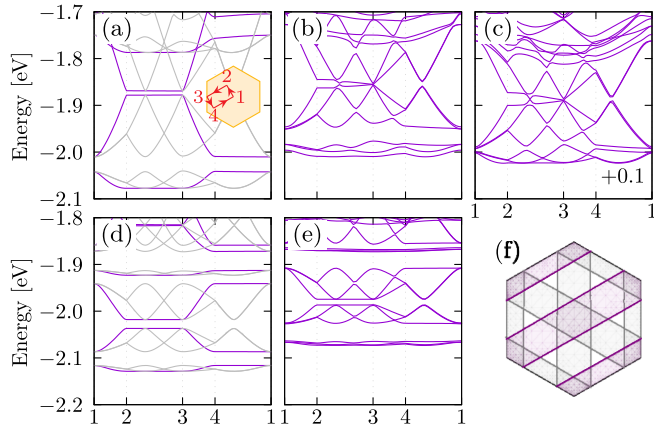
FIG. 7. Band structures for twisted bilayer BC_3. The path on which the band structures are drawn is shown as an inset in (a). The twist angle is $7.34°$ for (a)–(c) and $5.09°$ for (d) and (e). (a) and (d) are obtained with the bilayer $\mathbf{k} \cdot \mathbf{p}$ model. In (a) and (d), the purple lines are from the original M_1 point showing a signature of anisotropic band flattening, while the gray lines are from the original M_2 and M_3 points. (b) and (e) are obtained with the moiré tight-binding model, and (c) is from the large-scale DFT calculation performed using the OPENMX package. (f) The Fermi surfaces of the lowest energy band at half filling for the twist angle $7.34°$. As in the case for the band structures, the purple lines are contributed from the M_1 valley, while the gray lines are contributed from the M_2 and M_3 valleys.

continuum model, each valley can be treated separately, and the purple lines are from the M_1 valley, while the gray lines are contributed from the M_2 and M_3 valleys. Focusing on the purple lines, the low energy bands are dispersive in the 1-2 or 3-4 direction, but flat in the 1-4 or 2-3 direction. That is, we find valley-dependent anisotropic band flattening. Naming the dispersive direction the *easy direction* (since the electrons can move in this direction easily), the valley-dependent anisotropic band flattening is rephrased as the valley dependence of the easy direction. This valley-dependent quasi-1D feature is also seen in the isoenergy contour (Fermi energy) shown in Fig. 7(f). Considering the fact that $V^{(i)}(\mathbf{r})$ looks like the $90°$ rotated image of $V_{\kappa_i}(\boldsymbol{\tau})$ due to the action of $\boldsymbol{\tau}(\mathbf{r})$, the 1-2 and 3-4 direction corresponds to the direction in which $V^{(i)}(\mathbf{r})$ only weakly vary, while the 1-4 and 2-3 direction corresponds to the direction in which $V^{(i)}(\mathbf{r})$ strongly vary. This confirms the naive expectation that $V^{(i)}(\mathbf{r})$ act as a potential for electrons.

Then, for each valley, the system is regarded as a set of 1D channels aligned with the nanometer-scale spacing. Under the magnetic field, this in principle can host novel phases such as the fractional quantum Hall states discussed in the context of the coupled wire construction, depending on the interchannel interaction.

The electronic structure of the twisted bilayers can also be analyzed using the moiré tight-binding model. The Hamiltonian is Eq. (5), with the position of the p_z orbitals determined taking account of the relative angle mismatch and the corrugation $d_z(\boldsymbol{\tau}(\mathbf{r}))$. Figures 7(b) and 7(e) show the calculated band structures for $\phi = 7.34°$ and $5.09°$, respectively. These angles are chosen so that the periodicity of the microscopic

structure exactly matches the periodicity of the moiré pattern. In the moiré tight-binding description, the contributions from all three valleys, M_1 to M_3, come at once and are not strictly separable. Comparing Figs. 7(a) and 7(b) [or Figs. 7(d) and 7(e)], we can see that some degeneracies that originated from the decoupled valleys in the continuum model are lifted by the intervalley coupling in the tight-binding model. However, the band structures in the continuum model and the tight-binding model share the qualitative features. We expect that the intervalley coupling is rapidly killed in the small angle limit, because it requires a large momentum transfer, while the spatial dependence of the moiré pattern is relatively smooth. As we have noted, Eq. (12) is an approximation for the interlayer tunneling evaluated only up to the first order in $t_{\text{inter}}(\mathbf{r})$, and this is a possible source of the qualitative discrepancy between the continuum model and the tight-binding model other than the intervalley coupling.

In the case that the twist angle is relatively large, it is possible to apply the first-principles method on the large moiré unit cell. To handle the large moiré unit cell, here we employ the OPENMX package instead of the QUANTUM ESPRESSO package. Figure 7(c) shows the band structure for $\phi = 7.34°$ obtained using the same atomic coordinates as its moiré bilayer tight-binding counterpart. Now, we can see that the three approaches, the effective continuum model, the effective tight-binding model, and the large-scale DFT give not exactly the same, but consistent, band structures, which is remarkable considering the simplicity of the assumed $t_{\text{inter}}(\mathbf{r})$.

It is worth noting that the twist angle being much larger than the magic angle of graphene ($\sim 1°$) is sufficient to induce strong (anisotropic) band flattening here. Roughly speaking, a moiré pattern sets the length scale L. Within the local approximation, the interlayer tunneling $V(\mathbf{r})$, which essentially works as a potential, is scale invariant. On the other hand, the kinetic energy term scales as $1/L$ for the linear dispersion case of graphene while it scales as $1/L^2$ for the parabolic dispersion case here. This means that the potential term easily gets dominant over the kinetic term at smaller L (i.e., larger twist angle) for twisted bilayer BC_3.

D. Valley selection

As the valley-dependent anisotropic band flattening is promising for valleytronics applications, it is interesting to manipulate the valley population by external perturbations. Here, we show that linearly polarized light can induce valley population imbalance.

For simplicity, we compute the optical conductivity of the monolayer using the monolayer tight-binding model. The real part of the optical conductivity is computed as

$$\text{Re} \, \sigma_{\mu\mu}(\omega) = \sum_{\mathbf{k}} \left(\xi_{\mathbf{k}}^{\mu\mu}(\omega) - \xi_{\mathbf{k}}^{\mu\mu}(0) \right), \quad (15)$$

with

$$\xi_{\mathbf{k}}^{\mu\mu}(\omega) = -\frac{e^2}{\omega} \sum_{\alpha\beta} \frac{\left| \tilde{v}_{\mathbf{k},\alpha\beta}^{\mu} \right|^2 (f(E_{\mathbf{k}\alpha}) - f(E_{\mathbf{k}\beta})) \delta}{(\omega - (E_{\mathbf{k}\alpha} - E_{\mathbf{k}\beta}))^2 + \delta^2}, \quad (16)$$

where $\tilde{v}_{\mathbf{k},\alpha\beta}^{\mu}$ is the μ component of the velocity operator in the band diagonal basis and $E_{\mathbf{k}\alpha}$ is the band energy. To see the
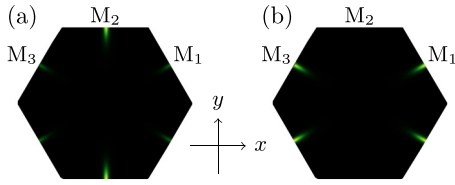
FIG. 8. Momentum dependence of (a) $\Xi_{xx}(\omega, \mathbf{k})$ and (b) $\Xi_{yy}(\omega, \mathbf{k})$ at $\hbar\omega = 1.5$ eV.

valley dependence, we focus on the integrand $\Xi_{\mu\mu}(\omega, \mathbf{k}) \equiv \xi_{\mathbf{k}}^{\mu\mu}(\omega) - \xi_{\mathbf{k}}^{\mu\mu}(0)$. Figure 8 shows the $\mathbf{k}$ dependence of the obtained $\Xi_{\mu\mu}(\omega, \mathbf{k})$ for $\omega = 1.5$ eV. Since we are now handling the monolayer model, the Brillouin zone is the original one, not the moiré Brillouin zone. Figures 8(a) and 8(b) are results for the cases with the light polarized in the x and y directions, respectively. The M_2 valley is bright in Fig. 8(a), while the M_1 and M_3 valleys are bright in Fig. 8(b), which clearly indicates the valley-dependent response. The symmetry analysis within DFT reveals that the irreducible representations for the highest energy valence band and the lowest energy conduction band at the M point are B_{3g} and B_{1u}, respectively. This explains the valley dependence in Fig. 8, since the function representations of B_{3g} and B_{1u} are yz and z, respectively. Note that the DFT results indicate that the monolayer BC₃ has an indirect band gap with the valence top at the Γ point contributed by the σ band, while the σ electrons are not included in our tight-binding model. Another note is that the standard DFT underestimates the gap size as we have noted and ω, to induce the valley imbalance, has to be adjusted to the experimental gap size.

E. Strongly correlated regime

The purple lines in Figs. 7(a) and 7(d) show that the lowest energy band in the effective continuum model is isolated from the other band. Here, we try to have an effective description of this specific band focusing on the strongly correlated regime. Due to the threefold valley degeneracy, we will end up with a three-orbital Hubbard model, where each orbital shows quasi-1D features associated with the valley-dependent easy direction. A similar model appeared in a previous study of generic twisted bilayers [24], leading to an interesting variant of the Kugel-Khomskii model in the strongly correlated limit. In the following, we derive the Kugel-Khomskii-like model for twisted bilayer BC₃.

Let us start with deriving a Hubbard model, which requires basis orbitals as well as hopping integrals and interaction parameters between them. For the basis orbitals and hoppings, we derive Wannier functions for the lowest energy band in the effective continuum model for each valley. This Wannier function should have a length scale of the moiré pattern rather than the scale of the atomic orbitals. The obtained Wannier functions (see Appendix D for the derivation) for the lowest energy bands in the M_1, M_2, and M_3 valleys at $\phi = 5.09°$ are shown in Figs. 9(a)–9(c), where the sum of the charge densities on both layers is plotted. They are well localized in the region where $|V_{\kappa_i}(\boldsymbol{\tau}(\mathbf{r}))|$ is large, and are elongated in the corresponding easy directions.
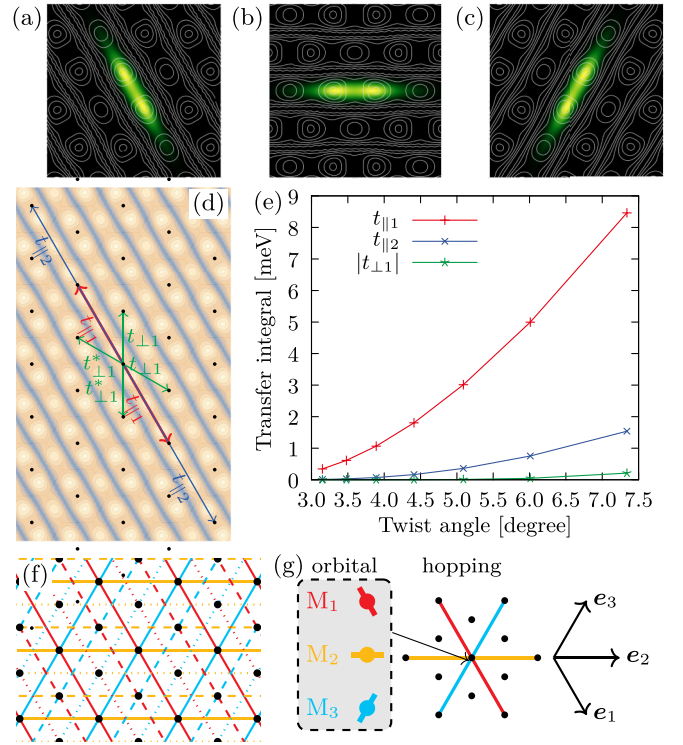

FIG. 9. (a)–(c) Wannier functions for the lowest band in the bilayer $\mathbf{k} \cdot \mathbf{p}$ model at $\theta = 5.09°$. (a), (b), and (c) are for the valleys from the original M_1, M_2, and M_3 points, respectively. The overlaid gray lines denote the contours of $|V(\mathbf{r})|$. (d) Definitions of the selected hopping integrals in the tight-binding model for the lowest band in the bilayer $\mathbf{k} \cdot \mathbf{p}$ model. The case of the M_1 valley is shown as an example. The background color map represents the contours of $|V(\mathbf{r})|$. (e) Angle dependence of the selected hopping integrals. (f) Nested network structure for the $t_{\|1}$-only model. Three networks shown by the solid, dashed, and dotted lines are decoupled with each other in terms of the hopping. If we further truncate the off-site Hubbard interactions, we can independently treat the three networks. (g) Schematic description of the ingredients in the minimal Hubbard model for one of the three networks. There are three orbitals, originally from the three valleys, and they hop in three different directions.

The major hoppings for the orbital from the M_1 valley are illustrated in Fig. 9(d). (The same thing for M_2 or M_3 can be obtained by rotating the picture appropriately.) As it should be, the major hoppings are along the easy direction. The major hoppings as functions of the twist angle are shown in Fig. 9(e). The smallness of $|t_{\perp 1}|$ signals the quasi-1D feature. Also, $t_{\|2}$ is significantly smaller than $t_{\|1}$, and thus keeping only $t_{\|1}$ is a reasonable approximation. In this approximation, each orbital forms a 1D chain only with the nearest-neighbor hopping, where the hopping direction depends on the orbitals. Note that if we turn off $t_{\perp 1}$ (and the other hoppings not along the easy direction), the system is decoupled into three nested triangular networks as is illustrated by the solid, dashed, and dotted lines in Fig. 9(f).

Now, let us move on to the electron-electron interaction terms, focusing on the on-site Coulomb repulsion between the Wannier orbitals for simplicity. The on-site interaction still preserves the decoupled nature of the three nested networks.
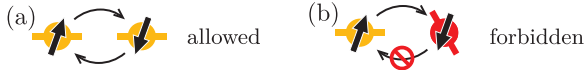
FIG. 10. Valley-dependent spin-spin coupling. When the same orbitals are aligned in the corresponding dispersive direction, it generates standard (super)exchange coupling (a). Otherwise, no spin exchange is generated (b).

Because of the elongated shapes of the Wannier functions [Figs. 9(a)–9(c)], the distinction between the intraorbital interaction U and the interorbital interaction U' is important. A rough estimation of U and U' is given by [15]

$$U_{\alpha\alpha'} = \frac{1}{(2\pi)^2} \int d^2\boldsymbol{q}\, \rho_{\alpha,\boldsymbol{q}} V_{\boldsymbol{q}} \rho_{\alpha',-\boldsymbol{q}}, \qquad (17)$$

with $U = U_{\alpha\alpha}$ and $U' = U_{\alpha\alpha'}$ ($\alpha \neq \alpha'$). Here, $V_{\boldsymbol{q}}$ is the Fourier components of the (screened) Coulomb interaction, and $\rho_{\alpha\boldsymbol{q}}$ is the sum of the charge densities in the upper and the lower layer for the orbital α.

Since the three nested networks are decoupled, we pick one of them from now on. Then, the effective Hubbard model becomes

$$H = t_{\|1} \sum_{\boldsymbol{r}\sigma} \sum_{\mu=1}^{3} c^\dagger_{\boldsymbol{r}+\boldsymbol{e}_\mu,\mu\sigma} c_{\boldsymbol{r},\mu\sigma} + \text{H.c.} + U \sum_{\boldsymbol{r}} \sum_{\mu=1}^{3} n_{\boldsymbol{r},\mu\uparrow} n_{\boldsymbol{r},\mu\downarrow}$$
$$+ U' \sum_{\boldsymbol{r},\sigma\sigma'} \sum_{\mu<\mu'} n_{\boldsymbol{r},\mu\sigma} n_{\boldsymbol{r},\mu'\sigma'}, \qquad (18)$$

where the orbital components and the definition of $\boldsymbol{e}_\mu$ are schematically illustrated in Fig. 9(g). Expanding in terms of $t_{\|1}/U$ and $t_{\|1}/U'$ to the lowest order (strongly correlated limit) at 1/6 filling, this Hamiltonian reduces to a variant of the Kugel-Khomskii model [49–51]

$$H = J \sum_{\boldsymbol{r}} \sum_{\mu=1}^{3} \left(\boldsymbol{S}_{\boldsymbol{r}+\boldsymbol{e}_\mu} \cdot \boldsymbol{S}_{\boldsymbol{r}} - \frac{1}{4} \right) \tilde{\tau}^{(\mu)}_{\boldsymbol{r}+\boldsymbol{e}_\mu} \tilde{\tau}^{(\mu)}_{\boldsymbol{r}}$$
$$- J' \sum_{\boldsymbol{r}} \sum_{\mu\neq\mu'} \left(\tilde{\tau}^{(\mu')}_{\boldsymbol{r}+\boldsymbol{e}_\mu} \tilde{\tau}^{(\mu)}_{\boldsymbol{r}} + \tilde{\tau}^{(\mu')}_{\boldsymbol{r}-\boldsymbol{e}_\mu} \tilde{\tau}^{(\mu)}_{\boldsymbol{r}} \right), \qquad (19)$$

with $J = 4t_{\|1}^2/U$, $J' = t_{\|1}^2/U'$, and $\tilde{\tau}^{(\mu)}$ being a 3×3 matrix in the orbital space defined as $(\tilde{\tau}^{(\mu)})_{ij} = \delta_{ij}\delta_{i\mu}$. In going from Eq. (18) to Eq. (19), it is important to note that the exchange is restricted by the orbital character, because an orbital only hops in its corresponding easy direction. For instance, when two orbitals are aligned as in Fig. 10(a), we expect textbook antiferromagnetic exchange interaction between the local spins [52]. On the other hand, when two orbitals are aligned as in Fig. 10(b), no spin exchange occurs. Namely, the up spin at the left site can hop to the right site, but the down spin at the right site cannot hop to the left site due to the orbital-dependent 1D nature. In the case of the original Kugel-Khomskii model [49–51], the orbital shapes account for the switching of the spin exchange, while here, the valley-dependent anisotropy accounts for the switching, showing the uniqueness of BC$_3$.

In Eq. (19), there is no term causing the orbital flip, which means that the orbital degrees of freedom are regarded as classical, allowing us to derive some eigenstates analytically. One example is a state with the ferro-orbital order (FOO),
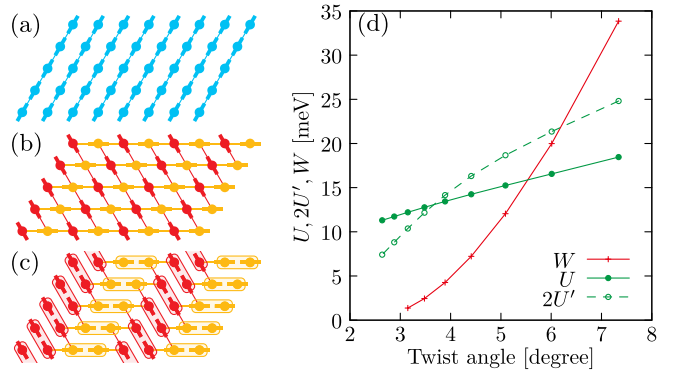

FIG. 11. (a)–(c) Selected eigenstates of Kugel-Khomskii-like model. (a) Ferro-orbital order (FOO). (b) Fully antiferro-orbital order (FAOO). (c) Dimer covering (DC). (d) Estimation of the Hubbard parameters U and U' by the Wannier function, compared with the bandwidth $W = 4t_{\|1}$.

where all the sites are in the same orbital state [Fig. 11(a)]. The Hamiltonian (19) indicates that the Heisenberg interaction (J term) works only in the easy direction of the selected orbital. Then, the FOO state is equivalent to the collection of the decoupled Heisenberg chains, and the lowest energy with FOO is obtained by the ground-state energy of the Heisenberg chain as [53]

$$E_{\text{per site}}^{\text{FOO}} \sim -0.69J. \qquad (20)$$

Note that this state is nematic, since Fig. 11(a) preserves the lattice translation symmetry but breaks the rotation symmetry. Another example is a state with the fully antiferro-orbital order (FAOO) depicted in Fig. 11(b). With this configuration, there are no active J bonds, and the energy is obtained from counting the active J' bonds, resulting in

$$E_{\text{per site}}^{\text{FAOO}} = -2J'. \qquad (21)$$

This state has a macroscopic number of degeneracy. Namely, any M_1 and M_2 orbitals in the state of Fig. 11(b) can be replaced by M_3 orbitals without energy cost, as far as the introduced M_3 orbitals induce no ferro-orbital coupling. The last example is a state with the dimer covering (DC) [Fig. 11(c)]. In this configuration, all the sites are paired to dimers by the J term, and the lowest energy with DC order is obtained by the energy of the spin singlet, resulting in

$$E_{\text{per site}}^{\text{DC}} = -J/2 - J'. \qquad (22)$$

This state also has macroscopic degeneracy, which can be checked by inserting M_3 dimers in Fig. 11(c). For both the FAOO and DC states, the macroscopic degeneracy will be lifted by quantum fluctuation induced by, for instance, the ring exchange that is derived as a higher-order correction to Eq. (19), and this will possibly lead to exotic quantum phases.

From the definitions of J and J', we have $E_{\text{per site}}^{\text{DC}} < E_{\text{per site}}^{\text{FOO}}$ for $U > U'$. We also have $E_{\text{per site}}^{\text{DC}} < E_{\text{per site}}^{\text{FAOO}}$ for $U < 2U'$, while $E_{\text{per site}}^{\text{DC}} > E_{\text{per site}}^{\text{FAOO}}$ for $U > 2U'$, i.e., there should be phase transitions controlled by U'/U.

Now, let us estimate U and U' by Eq. (17) with special attention to the ratio between U and $2U'$. For $V_{\boldsymbol{q}}$, we use

$$V_{\boldsymbol{q}} = \frac{2\pi k_0 e^2}{\bar{\epsilon} q} \tanh(q d_{\text{gate}}), \tag{23}$$

where $k_0 = 1/(4\pi\epsilon_0)$ and $\bar{\epsilon} = \epsilon/\epsilon_0$. This is for the case that the Coulomb interaction is screened by metallic gates above and below the system located d_{gate} off from the system [54–56]. Note that d_{gate} sets a length scale to the Coulomb interaction. In reality, we have to take care of all possible sources of screening, but here, for simplicity, we stick to Eq. (23) and treat ϵ as an adjustable parameter.

The Hubbard parameter U and $2U'$ computed with $\bar{\epsilon} = 10$ and $d_{\text{gate}} = 5$ nm are plotted as a function of the twist angle in Fig. 11(d), together with the estimated bandwidth $W = 4|t_{\parallel 1}|$. U and U' decrease much more slowly than W as the twist angle gets smaller, giving rise to a strongly correlated regime. Notably, there is a crossing between U and $2U'$. As Figs. 9(a)–9(c) show, the Wannier functions are elongated in the corresponding easy directions. In evaluating U', the two Wannier functions are misaligned, and thus U' is more sensitive to the length scale change than U, which explains the angle dependence of $2U'/U$.

IV. DISCUSSION

To summarize, twisted bilayer BC₃ is predicted to show valley-dependent anisotropic band flattening. This is an almost ideal realization of the notion that the quantum interference between Bloch wave functions in two layers leads to interesting band engineering in twisted bilayers. The valley-dependent anisotropic band flattening should be promising for valleytronics, and it is shown that the linearly polarized light induces valley imbalance.

Our analysis itself gives an important perspective on the theoretical and computational methodology for moiré systems. Namely, the current analysis serves as a working example of the cycle described in Fig. 3, where the intuitive understanding is available and the computational burden is avoided by the local approximation.

We also find a three-orbital Kugel-Khomskii-like model in the strongly correlated regime. The threefold degeneracy, originating from the suppressed intervalley scattering, is difficult to realize in conventional 2D materials, since there is no three-dimensional irreducible representation in 2D space groups (without the spin-orbit coupling), which highlights the uniqueness of BC₃. Indeed, some interesting eigenstates are derived, pointing towards exotic quantum phases. In a generic perspective, it is worth noting that not only U/W, but also U'/U can be controlled by the twist angle. This opens up a rich avenue to explore interesting quantum phases in multivalley moiré systems.

Regarding a quasi-1D state in twisted bilayers, there is an experimental report of a quasi-1D state in twisted bilayer tungsten ditelluride [57], and there is a theoretical prediction in twisted bilayer GeSe [58]. As we have just stated, the uniqueness of BC₃ over those former examples is a manifestation of the quantum interference and the Kugel-Khomskii model in the strongly correlated regime.

We would like to close the paper with a comment on the experimental realization. The monolayer BC₃ itself has already been synthesized [26]. Yet it can be a big challenge to apply the van der Waals stacking technique to this specific system. However, witnessing the rapid advances in the field, it will be realized in the near future.

APPENDIX A: TECHNICAL NOTES ON THE FIRST-PRINCIPLES CALCULATIONS

The first-principles calculations are performed mostly using the QUANTUM ESPRESSO package [59,60] with the required pseudopotentials from PSLIBRARY [61,62]. Only on one occasion, where we compare the band structures with moiré patterns obtained in the effective models and in the first-principles calculations, we employ the OPENMX package [63–66] in which the order-N calculations are implemented. Whenever the crystal structures are relevant [the lattice relaxation and the derivation of $d_z(\boldsymbol{\tau})$], rev-vdW-DF2 is used as a functional [67,68] to take into account the van der Waals interaction. In other cases, including the cases where the OPENMX package is employed, we use the PBE-GGA functional [69] for simplicity. In the crystal structure optimization, the atomic coordinates in the unit cell and the in-plane lattice constant are relaxed until the computed forces on each atom and the in-plane cell pressure go below 1.0×10^{-5} Ry/bohr and 5.0×10^{-2} kbar, respectively.

APPENDIX B: DERIVATION OF THE INTERLAYER DISTANCE

As we have noted, $d_z(\boldsymbol{\tau})$ is derived by maximizing the layer-layer binding energy with the crystalline parameters for each layer frozen. In practice, we set the period in the z direction to 40 Å and use the total energy for layer spacing $d_z = 20$ Å at $\boldsymbol{\tau} = 0$ as a reference energy to extract binding energy. (Note that $\boldsymbol{\tau}$ dependence is negligible at $d_z = 20$ Å.) Then, we plot the total energy as a function of the layer spacing for each $\boldsymbol{\tau}$ and find minima by fitting to [70]

$$E_{\text{total}}(d_z) = \alpha \exp\left(-\beta(d_z - d_{z0})\right) - \gamma(d_{z0}/d_z)^{4.5}. \tag{B1}$$

The fitting results for the selected $\boldsymbol{\tau}$ are shown in Fig. 12(a), and the contour plot of the obtained $d_z(\boldsymbol{\tau})$ is shown in Fig. 12(b) with the label "DFT." The exponent of the last term in Eq. (B1) could be adjusted to have better fittings, but Fig. 12(a) suggests that the long-tail behavior has a limited effect on the determination of the energy minimum. It turns out that $d_z(\boldsymbol{\tau})$ is satisfactory approximated by a
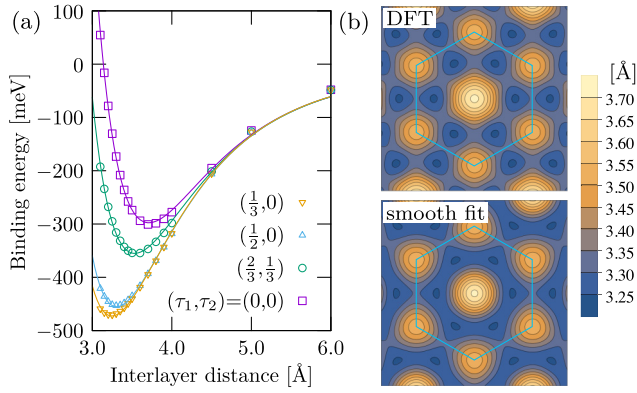
FIG. 12. (a) Interlayer distance dependence of the binding energy for selected $\tau = \tau_1 a_1 + \tau_2 a_2$. The optimized layer distance for each τ $d_z(\tau)$ is fixed by the binding energy minimum. (b) $d_z(\tau)$ obtained in the first-principles calculation (DFT) and corresponding smooth fit. The cyan hexagon denotes the unit cell.

simple function,

$$
\begin{aligned}
d_z(\tau) = c_1 + c_2(&\cos\tau_1 + \cos\tau_2 + \cos(\tau_1 - \tau_2)) \\
+ c_3(&\cos(\tau_1 + \tau_2) + \cos(\tau_1 - 2\tau_2) + \cos(2\tau_1 - \tau_2)) \\
+ c_4(&\cos(2\tau_1) + \cos(2\tau_2) + \cos(2\tau_1 - 2\tau_2)), \quad \text{(B2)}
\end{aligned}
$$

with $\{c_1, c_2, c_3, c_4\} = \{3.361 \text{ Å}, 0.025 \text{ Å}, 0.077 \text{ Å}, 0.015 \text{ Å}\}$, whose contour plot is shown in Fig. 12(b) with the label "smooth fit." We can see that this function nicely compares with the DFT result.

APPENDIX C: CONSTRUCTING WANNIER FUNCTIONS FOR A MONOLAYER

The Wannier functions for the bands near the Fermi energy in monolayer BC_3 are derived using the WANNIER90 package [48]. Specifically, we build a tight-binding model for π electrons, and for this purpose, we put eight p_z-like orbitals on the six C sites and the two B sites in the unit cell as an initial guess for the Wannier functions. We set the inner energy window, which selects an energy range where the DFT band structure is faithfully reproduced by the tight-binding model, from -2.07 to 1.63 eV.

APPENDIX D: CONSTRUCTING MOIRÉ SCALE WANNIER FUNCTIONS TO ACCESS THE STRONGLY CORRELATED REGIME

The Wannier function for the lowest energy band in the continuum model for the twisted bilayer BC_3 is derived by projecting a candidate wave function to the subspace spanned by the lowest energy band, as is done in preparing an initial guess in the well-known algorithm for the maximally localized Wannier function [47]. In our case, since the lowest energy band is well separated from the other bands, this "initial guess" is already well localized if we choose a proper candidate wave function, and we will use it as a Wannier function. In practice, a Gaussian function whose decay length is $|L_i|/10$ placed at the unit cell center is used as a candidate function for both the upper and the lower layer but with the opposite sign.

[1] A. K. Geim and I. V. Grigorieva, Van der Waals heterostructures, Nature (London) **499**, 419 (2013).

[2] J. M. B. Lopes dos Santos, N. M. R. Peres, and A. H. Castro Neto, Graphene Bilayer with a Twist: Electronic Structure, Phys. Rev. Lett. **99**, 256802 (2007).

[3] G. Trambly de Laissardière, D. Mayou, and L. Magaud, Localization of Dirac electrons in rotated graphene bilayers, Nano Lett. **10**, 804 (2010).

[4] G. Li, A. Luican, J. M. B. Lopes dos Santos, A. H. Castro Neto, A. Reina, J. Kong, and E. Y. Andrei, Observation of Van Hove singularities in twisted graphene layers, Nat. Phys. **6**, 109 (2010).

[5] E. J. Mele, Commensuration and interlayer coherence in twisted bilayer graphene, Phys. Rev. B **81**, 161405(R) (2010).

[6] E. Suárez Morell, J. D. Correa, P. Vargas, M. Pacheco, and Z. Barticevic, Flat bands in slightly twisted bilayer graphene: Tight-binding calculations, Phys. Rev. B **82**, 121407(R) (2010).

[7] R. Bistritzer and A. H. MacDonald, Moiré bands in twisted double-layer graphene, Proc. Natl. Acad. Sci. U. S. A. **108**, 12233 (2011).

[8] A. Luican, G. Li, A. Reina, J. Kong, R. R. Nair, K. S. Novoselov, A. K. Geim, and E. Y. Andrei, Single-Layer Behavior and Its Breakdown in Twisted Graphene Layers, Phys. Rev. Lett. **106**, 126802 (2011).

[9] P. Moon and M. Koshino, Energy spectrum and quantum Hall effect in twisted bilayer graphene, Phys. Rev. B **85**, 195458 (2012).

[10] J. M. B. Lopes dos Santos, N. M. R. Peres, and A. H. Castro Neto, Continuum model of the twisted graphene bilayer, Phys. Rev. B **86**, 155449 (2012).

[11] D. Wong, Y. Wang, J. Jung, S. Pezzini, A. M. DaSilva, H.-Z. Tsai, H. S. Jung, R. Khajeh, Y. Kim, J. Lee, S. Kahn, S. Tollabimazraehno, H. Rasool, K. Watanabe, T. Taniguchi, A. Zettl, S. Adam, A. H. MacDonald, and M. F. Crommie, Local spectroscopy of moiré-induced electronic structure in gate-tunable twisted bilayer graphene, Phys. Rev. B **92**, 155409 (2015).

[12] K. Kim, A. DaSilva, S. Huang, B. Fallahazad, S. Larentis, T. Taniguchi, K. Watanabe, B. J. LeRoy, A. H. MacDonald, and E. Tutuc, Tunable moiré bands and strong correlations in small-twist-angle bilayer graphene, Proc. Natl. Acad. Sci. U. S. A. **114**, 3364 (2017).

[13] Y. Cao, V. Fatemi, A. Demir, S. Fang, S. L. Tomarken, J. Y. Luo, J. D. Sanchez-Yamagishi, K. Watanabe, T. Taniguchi, E. Kaxiras, R. C. Ashoori, and P. Jarillo-Herrero, Correlated insulator behaviour at half-filling in magic-angle graphene superlattices, Nature (London) **556**, 80 (2018).

[14] Y. Cao, V. Fatemi, S. Fang, K. Watanabe, T. Taniguchi, E. Kaxiras, and P. Jarillo-Herrero, Unconventional superconductivity in magic-angle graphene superlattices, Nature (London) **556**, 43 (2018).

[15] M. Koshino, N. F. Q. Yuan, T. Koretsune, M. Ochi, K. Kuroki, and L. Fu, Maximally Localized Wannier Orbitals and the

Extended Hubbard Model for Twisted Bilayer Graphene, Phys. Rev. X **8**, 031087 (2018).

[16] A. L. Sharpe, E. J. Fox, A. W. Barnard, J. Finney, K. Watanabe, T. Taniguchi, M. A. Kastner, and D. Goldhaber-Gordon, Emergent ferromagnetism near three-quarters filling in twisted bilayer graphene, Science **365**, 605 (2019).

[17] X. Lu, P. Stepanov, W. Yang, M. Xie, M. A. Aamir, I. Das, C. Urgell, K. Watanabe, T. Taniguchi, G. Zhang, A. Bachtold, A. H. MacDonald, and D. K. Efetov, Superconductors, orbital magnets and correlated states in magic-angle bilayer graphene, Nature (London) **574**, 653 (2019).

[18] M. Yankowitz, S. Chen, H. Polshyn, Y. Zhang, K. Watanabe, T. Taniguchi, D. Graf, A. F. Young, and C. R. Dean, Tuning superconductivity in twisted bilayer graphene, Science **363**, 1059 (2019).

[19] D. Wong, K. P. Nuckolls, M. Oh, B. Lian, Y. Xie, S. Jeon, K. Watanabe, T. Taniguchi, B. A. Bernevig, and A. Yazdani, Cascade of electronic transitions in magic-angle twisted bilayer graphene, Nature (London) **582**, 198 (2020).

[20] U. Zondiner, A. Rozen, D. Rodan-Legrain, Y. Cao, R. Queiroz, T. Taniguchi, K. Watanabe, Y. Oreg, F. von Oppen, A. Stern, E. Berg, P. Jarillo-Herrero, and S. Ilani, Cascade of phase transitions and Dirac revivals in magic-angle graphene, Nature (London) **582**, 203 (2020).

[21] M. Serlin, C. L. Tschirhart, H. Polshyn, Y. Zhang, J. Zhu, K. Watanabe, T. Taniguchi, L. Balents, and A. F. Young, Intrinsic quantized anomalous Hall effect in a moiré heterostructure, Science **367**, 900 (2020).

[22] K. P. Nuckolls, M. Oh, D. Wong, B. Lian, K. Watanabe, T. Taniguchi, B. A. Bernevig, and A. Yazdani, Strongly correlated Chern insulators in magic-angle twisted bilayer graphene, Nature (London) **588**, 610 (2020).

[23] Y. Choi, H. Kim, Y. Peng, A. Thomson, C. Lewandowski, R. Polski, Y. Zhang, H. S. Arora, K. Watanabe, T. Taniguchi, J. Alicea, and S. Nadj-Perge, Correlation-driven topological phases in magic-angle twisted bilayer graphene, Nature (London) **589**, 536 (2021).

[24] T. Kariyado and A. Vishwanath, Flat band in twisted bilayer Bravais lattices, Phys. Rev. Res. **1**, 033076 (2019).

[25] A. Rycerz, J. Tworzydlo, and C. W. J. Beenakker, Valley filter and valley valve in graphene, Nat. Phys. **3**, 172 (2007).

[26] H. Tanaka, Y. Kawamata, H. Simizu, T. Fujita, H. Yanagisawa, S. Otani, and C. Oshima, Novel macroscopic BC$_3$ honeycomb sheet, Solid State Commun. **136**, 22 (2005).

[27] H. Yanagisawa, Y. Ishida, T. Tanaka, A. Ueno, S. Otani, and C. Oshima, Metastable BC$_3$ honeycomb epitaxial sheets on the NbB$_2$(0001) surface, Surf. Sci. **600**, 4072 (2006).

[28] H. Yanagisawa, T. Tanaka, Y. Ishida, M. Matsue, E. Rokuta, S. Otani, and C. Oshima, Phonon Dispersion Curves of a BC$_3$ Honeycomb Epitaxial Sheet, Phys. Rev. Lett. **93**, 177003 (2004).

[29] A. Ueno, T. Fujita, M. Matsue, H. Yanagisawa, C. Oshima, F. Patthey, H.-C. Ploigt, W.-D. Schneider, and S. Otani, Scanning tunneling microscopy study on a BC$_3$ covered NbB$_2$(0001) surface, Surf. Sci. **600**, 3518 (2006).

[30] R. M. Wentzcovitch, M. L. Cohen, S. G. Louie, and D. Tománek, σ-states contribution to the conductivity of BC$_3$, Solid State Commun. **67**, 515 (1988).

[31] Y. Miyamoto, A. Rubio, S. G. Louie, and M. L. Cohen, Electronic properties of tubule forms of hexagonal BC$_3$, Phys. Rev. B **50**, 18360 (1994).

[32] S. Behzad, Mechanical control of the electro-optical properties of monolayer and bilayer BC$_3$ by applying the in-plane biaxial strain, Surf. Sci. **665**, 37 (2017).

[33] H. Zhang, Y. Liao, G. Yang, and X. Zhou, Theoretical studies on the electronic and optical properties of honeycomb BC$_3$ monolayer: A promising candidate for metal-free photocatalysts, ACS Omega **3**, 10517 (2018).

[34] H. Wang, Q. Li, H. Pan, Y. Gao, and M. Sun, Comparative investigation of the mechanical, electrical and thermal transport properties in graphene-like C$_3$B and C$_3$N, J. Appl. Phys. **126**, 234302 (2019).

[35] Y. Wu, W. Xia, Y. Zhang, W. Zhu, W. Zhang, and P. Zhang, Remarkable Band-Gap Renormalization via Dimensionality of the Layered Material C$_3$B, Phys. Rev. Appl. **14**, 014073 (2020).

[36] Z. Wang, Z. Luo, J. Li, K. Yang, and G. Zhou, 2D van der Waals heterostructures of graphitic BCN as direct Z-scheme photocatalysts for overall water splitting: the role of polar π-conjugated moieties, Phys. Chem. Chem. Phys. **22**, 23735 (2020).

[37] M. Fujimoto and T. Kariyado, Effective continuum model of twisted bilayer GeSe and origin of the emerging one-dimensional mode, Phys. Rev. B **104**, 125427 (2021).

[38] J. Jung, A. Raoux, Z. Qiao, and A. H. MacDonald, *Ab initio* theory of moiré superlattice bands in layered two-dimensional materials, Phys. Rev. B **89**, 205414 (2014).

[39] K. Uchida, S. Furuya, J.-I. Iwata, and A. Oshiyama, Atomic corrugation and electron localization due to moiré patterns in twisted bilayer graphenes, Phys. Rev. B **90**, 155451 (2014).

[40] R. Akashi, Y. Iida, K. Yamamoto, and K. Yoshizawa, Interference of the Bloch phase in layered materials with stacking shifts, Phys. Rev. B **95**, 245401 (2017).

[41] P. Moon and M. Koshino, Optical absorption in twisted bilayer graphene, Phys. Rev. B **87**, 205404 (2013).

[42] Y. Wang, Z. Wang, W. Yao, G.-B. Liu, and H. Yu, Interlayer coupling in commensurate and incommensurate bilayer structures of transition-metal dichalcogenides, Phys. Rev. B **95**, 115429 (2017).

[43] F. Rost, R. Gupta, M. Fleischmann, D. Weckbecker, N. Ray, J. Olivares, M. Vogl, S. Sharma, O. Pankratov, and S. Shallcross, Nonperturbative theory of effective Hamiltonians for deformations in two-dimensional materials: Moiré systems and dislocations, Phys. Rev. B **100**, 035101 (2019).

[44] D. Tomanek, R. M. Wentzcovitch, S. G. Louie, and M. L. Cohen, Calculation of electronic and structural properties of BC$_3$, Phys. Rev. B **37**, 3134 (1988).

[45] X. Lin and J. Ni, Electronic and magnetic properties of substitutionally Fe-, Co-, and Ni-doped BC$_3$ honeycomb structure, J. Appl. Phys. **111**, 034309 (2012).

[46] X. Tan, P. Jin, and Z. Chen, With the same Clar formulas, do the two-dimensional sandwich nanostructures X–Cr–X (X = C$_4$H, NC$_3$ and BC$_3$) behave similarly? Phys. Chem. Chem. Phys. **16**, 6002 (2014).

[47] N. Marzari and D. Vanderbilt, Maximally localized generalized Wannier functions for composite energy bands, Phys. Rev. B **56**, 12847 (1997).

[48] G. Pizzi, V. Vitale, R. Arita, S. Blügel, F. Freimuth, G. Géranton, M. Gibertini, D. Gresch, C. Johnson, T. Koretsune, J. Ibañez-Azpiroz, H. Lee, J.-M. Lihm, D. Marchand, A.

Marrazzo, Y. Mokrousov, J. I. Mustafa, Y. Nohara, Y. Nomura, L. Paulatto *et al.*, Wannier90 as a community code: new features and applications, J. Phys.: Condens. Matter **32**, 165902 (2020).

[49] K. I. Kugel and D. I. Khomski, The Jahn-Teller effect and magnetism: transition metal compounds, Sov. Phys.-Usp. **25**, 231 (1982).

[50] G. Khaliullin and V. Oudovenko, Spin and orbital excitation spectrum in the Kugel-Khomskii model, Phys. Rev. B **56**, R14243 (1997).

[51] F. Wang and A. Vishwanath, Z_2 spin-orbital liquid state in the square lattice Kugel-Khomskii model, Phys. Rev. B **80**, 064413 (2009).

[52] P. W. Anderson, New approach to the theory of superexchange interactions, Phys. Rev. **115**, 2 (1959).

[53] T. Giamarchi, *Quantum Physics in One Dimension* (Clarendon, Oxford, 2003).

[54] T. Cea, N. R. Walet, and F. Guinea, Electronic band structure and pinning of Fermi energy to Van Hove singularities in twisted bilayer graphene: A self-consistent approach, Phys. Rev. B **100**, 205113 (2019).

[55] J. Kang and O. Vafek, Non-Abelian Dirac node braiding and near-degeneracy of correlated phases at odd integer filling in magic-angle twisted bilayer graphene, Phys. Rev. B **102**, 035161 (2020).

[56] T. Cea and F. Guinea, Band structure and insulating states driven by Coulomb interaction in twisted bilayer graphene, Phys. Rev. B **102**, 045107 (2020).

[57] P. Wang, G. Yu, Y. H. Kwan, Y. Jia, S. Lei, S. Klemenz, F. A. Cevallos, R. Singha, T. Devakul, K. Watanabe, T. Taniguchi, S. L. Sondhi, R. J. Cava, L. M. Schoop, S. A. Parameswaran, and S. Wu, One-dimensional Luttinger liquids in a two-dimensional moiré lattice, Nature (London) **605**, 57 (2022).

[58] D. M. Kennes, L. Xian, M. Claassen, and A. Rubio, One-dimensional flat bands in twisted bilayer germanium selenide, Nat. Commun. **11**, 1124 (2020).

[59] P. Giannozzi, S. Baroni, N. Bonini, M. Calandra, R. Car, C. Cavazzoni, D. Ceresoli, G. L. Chiarotti, M. Cococcioni, I. Dabo, A. D. Corso, S. de Gironcoli, S. Fabris, G. Fratesi, R. Gebauer, U. Gerstmann, C. Gougoussis, A. Kokalj, M. Lazzeri, L. Martin-Samos *et al.*, QUANTUM ESPRESSO: a modular and open-source software project for quantum simulations of materials, J. Phys.: Condens. Matter **21**, 395502 (2009).

[60] P. Giannozzi, O. Andreussi, T. Brumme, O. Bunau, M. B. Nardelli, M. Calandra, R. Car, C. Cavazzoni, D. Ceresoli, M. Cococcioni, N. Colonna, I. Carnimeo, A. D. Corso, S. de Gironcoli, P. Delugas, R. A. DiStasio, A. Ferretti, A. Floris, G. Fratesi, G. Fugallo *et al.*, Advanced capabilities for materials modelling with Quantum ESPRESSO, J. Phys.: Condens. Matter **29**, 465901 (2017).

[61] https://dalcorso.github.io/pslibrary/.

[62] A. Dal Corso, Pseudopotentials periodic table: From H to Pu, Comput. Mater. Sci. **95**, 337 (2014).

[63] https://www.openmx-square.org.

[64] T. Ozaki, Variationally optimized atomic orbitals for large-scale electronic structures, Phys. Rev. B **67**, 155108 (2003).

[65] T. Ozaki and H. Kino, Numerical atomic basis orbitals from H to Kr, Phys. Rev. B **69**, 195113 (2004).

[66] T. Ozaki and H. Kino, Efficient projector expansion for the *ab initio* LCAO method, Phys. Rev. B **72**, 045121 (2005).

[67] T. Thonhauser, V. R. Cooper, S. Li, A. Puzder, P. Hyldgaard, and D. C. Langreth, Van der Waals density functional: Self-consistent potential and the nature of the van der Waals bond, Phys. Rev. B **76**, 125112 (2007).

[68] I. Hamada, van der Waals density functional made accurate, Phys. Rev. B **89**, 121103(R) (2014).

[69] J. P. Perdew, K. Burke, and M. Ernzerhof, Generalized Gradient Approximation Made Simple, Phys. Rev. Lett. **77**, 3865 (1996).

[70] C.-R. Hsing, C. Cheng, J.-P. Chou, C.-M. Chang, and C.-M. Wei, Van der Waals interaction in a boron nitride bilayer, New J. Phys. **16**, 113015 (2014).